Experimental determination of real elements of the density matrix and the dipole moment of H($n = 3$) atoms produced from 20–100-keV H$^+$ on Ar

S. P. Renwick, E. C. Martell,* W. D. Weaver,† and J. S. Risley

Atomic Collisions Laboratory, Department of Physics, North Carolina State University, Raleigh, North Carolina 27695-8202

Diagonal and real off-diagonal coherence elements of the density matrix for H($n = 3$) atoms produced in 20–100-keV electron-capture collisions of protons with Ar atoms are experimentally determined. Balmer-α light from the decay of H atoms from the ($n = 3$) state to the ($n = 2$) state is observed. The intensity and polarization of the light as a function of an axially symmetric electric field in the collision region are fitted to a numerical model of the H atom in an electric field in order to extract density-matrix elements. A new polarimeter, using a photoelastic modulator in conjunction with photon-counting techniques, is used in the experiment, and its efficacy is analyzed and compared to that of a rotating quarter-wave plate polarimeter previously used in similar experiments. The diagonal elements of the density matrix yield relative capture cross sections for the H($3l$) angular-momentum substates, while the coherence terms are used to determine the dipole moment of the atoms produced. Results are compared to those for protons colliding with a He target and the differences are discussed.

I. INTRODUCTION

We present results of a study of formation of H($n = 3$) atoms by electron capture from an Ar target by 20–100-keV protons. We use an apparatus similar to that employed in previous work concerning formation of H($n = 3$) atoms [1–3] and H($n = 2$) atoms [4] by electron capture from He targets, in which precision polarimeters were used to analyze the Balmer-α and Lyman-α light emitted by the radiative decay of the H atoms. In the present work we extend the range of applicability of our experimental techniques by using a new polarimeter and a procedure for eliminating background-light contributions from excited Ar target atoms. This allows us to compare production of H($n = 3$) atoms from different target species.

The formation of excited states of the H atom by electron capture has been extensively studied, with older work reviewed by Brouillard in 1981 [5]. Except for studies involving Rydberg-atom formation, work has concentrated mainly on the H($n = 2$) and H($n = 3$) states. While older work was chiefly concerned with measuring cross sections for angular-momentum substates [e.g., for H($3s$), H($3p$), and H($3d$)], more recently it has been possible to use the polarization of the light emitted by radiative decay to extract additional information about coherences between substates of the excited atom produced in the collision. Some examples of other experimenters' work that are relevant to the present study are mentioned below, but the list here is not exhaustive. The subject has been reviewed by Hippler [6,7]. As the H atom is not produced in an angular-momentum eigenstate in the collision, cross sections for H(nl) eigenstates do not include all the possible information about the state produced. A complete description of the atoms is given by a density matrix [8], whose diagonal elements are equal to the (relative) partial cross sections for H(nl) eigenstates and whose off-diagonal elements describe coherences between the angular-momentum substates coherently produced in the collision. Knowledge of these off-diagonal elements allows calculation of certain properties of the excited H atom produced, such as its electric dipole moment.

Work concerning the production of H($n = 2$) atoms requires polarization measurements of UV Lyman-α radiation (1216 Å) and is therefore challenging. Here, recently, cross sections for production of H($2s$) by electron capture from rare-gas targets have been measured by Cline, Westerveld, and Risley from 20 to 100 keV [4], by Hippler *et al.* between 1 and 25 keV [9], and by Van Zyl, Gealy, and Neumann below 2 keV [10]. Hippler *et al.* have also determined electric dipole moments of H($n = 2$) atoms produced in a He target [11], and Tepehan *et al.* have performed a similar study for Ne and Ar targets [12].

Similar experiments concerning H($n = 3$) atoms are generally easier, involving measurement of visible Balmer-α radiation (6562 Å). Cross sections for Balmer-α emission were measured by Van Zyl, Rothwell, and Neumann for an Ar target [13] and for the other rare gases [14]. Cross sections for capture to the $3p$ state by 2–15-keV protons on Ar were measured by Risley, de Heer, and Kerkdijk [15]. Capture cross sections to the $3s$, $3p$, and $3d$ states for 10–120-keV protons on Ar and other targets were measured by Hughes *et al.* [16]. The cross sections for population of H($3l$) states from a He target were measured recently by Brower and Pipkin using a microwave-resonance technique [17].

This laboratory has concentrated on the determination of density matrices for H atoms from 20–100-keV protons colliding with a He target [3,4]. The procedure for doing so is as follows: The electron capture takes place in an electric field weak enough to leave the capture process unaffected but strong enough to mix angular-momentum substates via the Stark effect. Both the intensity and the

polarization of the light emitted in radiative decay are measured with a precision polarimeter, which is used to determine the Stokes parameters of the light as a function of the electric field. Intensity variation with electric field will be caused by Stark mixing of states with different lifetimes. Variation in the polarization of the light with electric field will also be expected, as each decaying state has its own "signature" polarization fraction.

The measured Stokes parameters then yield the density matrix of the H atoms in the following manner: For $H(n=3)$, under the conditions of our experiment, there are 14 independent nonzero density-matrix elements, or 14 linearly independent basis states with which to describe the H atom. The expected contribution to the Stokes parameters from each of the independent states is separately calculated by numerical integration of the Schrödinger equation. This calculation involves known dynamical behavior of the H atom in an electric field and is believed to be accurate. Statistical fitting of the experimental data to the calculated Stokes parameters allows us to determine the contributions from the different substates and thus find the density matrix.

Density-matrix elements for $H(n=3)$ were found by this method initially by Havener and co-workers [18] and later remeasured with improved accuracy and precision by Ashburn et al. [2,3]. Cross sections for $H(3l)$ production were determined to high accuracy by Cline, Westerveld, and Risley [19]. Density matrices for the $H(n=2)$ atom have been measured by Cline, Westerveld, and Risley [4].

In an effort to observe possible scaling laws concerning electron capture from different rare-gas targets, we have now determined the diagonal elements and real off-diagonal elements of the density matrix for $H(n=3)$ atoms formed in 20–100-keV collisions of protons with Ar. This required development of an accurate procedure for subtracting the effects of light emitted by excited target Ar atoms. We have improved the apparatus by employing a new polarimeter that incorporates a photoelastic modulator (PEM) and photon-counting electronics. The PEM eliminates the use of nonlinear fitting [2] to extract Stokes parameters and enables us to easily apply our background subtraction. While PEM devices have been extensively used in astronomical experiments, this is, we believe, the first use of a PEM in an atomic-collisions experiment. The performance of, and possible systematic errors inherent to, the PEM polarimeter will be discussed, and results obtained with it for a He target will be compared to previous results. The density-matrix elements mentioned above for the Ar target, along with the dipole moment of the $H(n=3)$ atom formed, will be presented and discussed.

II. APPARATUS

A. General

The apparatus used in these experiments has previously been extensively described [2,18], so only a brief outline of it will be given here. The new polarimeter will be described in detail in Sec. II B.

Protons are produced in a duoplasmatron ion source, extracted, and accelerated to energies between 20 and 100 keV. The beam is focused by an electrostatic einzel lens and quadrupole magnet before entering the dipole field of a bending magnet used for mass separation. Three pairs of electric-field plates are employed to steer the beam. A phosphor screen can be used to observe the beam spot in order to optimize beam characteristics. Beam currents, measured by a Faraday cup, were usually about 1–2 μA at the end of the line, although beam current dropped off sharply at the lower energies, reaching ~0.2 μA at 20 keV.

The protons are then sent into the collision region shown in Fig. 1. Before entering the target cell, shown at the center of the diagram, the beam is collimated by two apertures 0.16 cm in diameter and 26 cm apart, not shown in the diagram. Ar or He gas for the collision is fed in at the end of the chamber through a precision leak valve, immersing the entire back part of the chamber, including the Faraday cup, in the target gas. The entrance aperture of the cell serves to isolate the collision region from the front part of the chamber. Cell pressure is determined absolutely by a capacitance manometer that measures the pressure difference between the front and
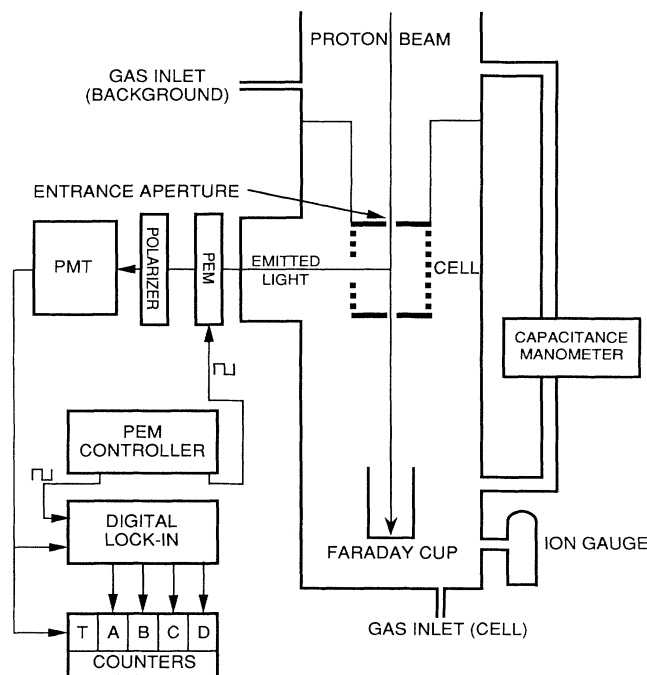

FIG. 1. The experimental apparatus. 20–100-keV protons enter the collision chamber from the top of the diagram. A microcomputer, not shown, applies voltages from a programmable high-voltage supply to the ten electrodes shown forming the central collision region in order to produce the desired axial electric field in the cell. Balmer-α light emitted from the collision cell is collected by a system of two lenses, not shown in the figure, and analyzed by the polarimeter consisting of the PEM and linear polarizer. The computer collects signals from the counters, the Faraday cup, and the ion gauge and analyzes them as described in the text to obtain Stokes parameters of the light emitted from the collision.

back of the chamber. This pressure is maintained at 1.0±0.03 mTorr for He and 0.24±0.01 mTorr for Ar, which keeps the variation of ion beam current with target pressure well into the linear regime, thus ensuring single-collision conditions. The pressure in the front is maintained at 5×10^{-6} Torr or less via differential pumping.

Balmer-α light emitted from excited H atoms in the target cell is observed via photon counting by the optical detection system shown at the left of Fig. 1. Collisions with background gas in front of the target cell can present a significant background contribution to the optical signal, as H atoms produced well ahead of the cell can live long enough to decay in view of the detection system. To correct for this background, an automated subtraction technique, described in detail in Ref. [2], is used. Target gas is periodically routed to the region upstream of the cell, and the difference is taken between signals measured both with gas in the cell and gas admitted upstream of the cell. This ensures that we observe light from decays taking place in the desired collision region. Collisions with target gas issuing from the entrance aperture are accounted for as described below.

In order to account for pressure changes in this background subtraction and for possible beam drifts, optical signals are normalized to both the beam current, integrated during the measurement time from the Faraday cup, and to cell pressure, determined from integration of the current from an ion gauge. A correction for the 5–10 % beam attenuation occurring with target gas in the cell has been measured with ±10% precision and is included in the data analysis.

We measure the intensity and polarization of the Balmer-α light as a function of the electric field applied in the target cell. While in our previous experiments both an axial and a transverse electric field were applied to the atoms, in the current study only an axial field is employed. The primary motive for this work is to find the dipole moment of the H atoms, for which the axial field measurement is sufficient. The cell is 54.0±0.1 mm long with a radius of 38.1 mm. Opposite-polarity voltages of equal magnitude are applied to the cell entrance and exit apertures, and a system of eight rings, between the apertures and connected to them with a string of precision resistors, maintains a uniform potential drop along the cell axis with zero potential at the center. Fields of ±277.67 V/cm or less are used, requiring voltages of ±1080 V or less on the apertures. These voltages are applied by a precision programmable power supply. An additional field plate is located before the entrance aperture and biased to maintain approximately the same electric field before the cell as in it. This helps to minimize effects of nonuniform fields before the cell and also keeps atoms formed immediately before the cell in the same electric field as the desired atoms. The effect of this additional plate is included in the data analysis. A 10.5-mm hole is cut in one side of the cell to allow observation of the emitted Balmer-α light.

We fit the data to a model of the behavior of the H atom in the electric field. This requires precise knowledge of the variation in the electric field in the cell, which has been obtained by a relaxation-method calcula-

tion [2]. All the effects outlined above are included, although the effect of the 10.5-mm hole is assumed to be negligible.

B. The PEM polarimeter: determination of Stokes parameters

1. Principles of operation

We quantify the measurement of light intensity and polarization by use of the Stokes parameters

$$S_0 = I_{\parallel} + I_{\perp} ,$$

$$S_1 = I_{\parallel} - I_{\perp} ,$$

$$S_2 = I_{45°} - I_{135°} , \qquad (2.1)$$

$$S_3 = I_{rh} - I_{lh} .$$

Here $I_{\parallel}$ and $I_{\perp}$ denote light intensity polarized parallel and perpendicular to the beam axis, respectively; $I_{45°}$ and $I_{135°}$ denote intensity polarized at their respective angles to the beam axis; and I_{rh} and I_{lh} denote right-handed and left-handed circularly polarized light. We define the z axis as the beam axis and the y axis as pointing out of the collision region toward the optical system.

Previous measurements of H($n=3$) density matrices in this laboratory [3] used a polarimeter consisting of a stationary linear polarizer and rotating Balmer-α quarter-wave plate. A nonlinear statistical fit was performed to the intensity of light emitted as a function of wave-plate angle in order to find the Stokes parameters of the light. We wished to simplify this system and allow easier measurements of polarization of other atomic transitions. We now employ a polarimeter including a photoelastic modulator [20].

The PEM contains a rectangular fused-silica plate excited into a vibration mode by an attached piezoelectric crystal. The voltage applied to the piezoelectric is sinusoidal, setting up a standing wave in the crystal, and the accompanying sinusoidally varying strain in the PEM crystal gives it a time-varying retardation:

$$\Delta = (\Delta_0 \sin \omega t + \delta) \cos \left[\frac{\pi x'}{l} \right] , \qquad (2.2)$$

where the oscillation is at frequency ω and the cosine term accounts for spatial variation in Δ along the crystal oscillation axis (the x' axis). In our experiment, the oscillation frequency $\omega/2\pi$ is equal to 50 kHz. The retardation amplitude Δ_0 is controlled by the piezoelectric crystal's voltage and is simply set by a dial, so the device is very versatile. The dc δ term accounts for any inherent retardation in the crystal. It was recognized [21,22] that such a crystal will impose a sinusoidally varying modulation to the polarization of light passed through it. This allows one to use lock-in techniques to extract a small polarization signal from a large background.

The PEM is set up as shown in Fig. 2. Light from the experiment, after being filtered by an interference filter with 100-Å bandpass centered at 6562 Å, is passed through the PEM crystal with its oscillation axis at 45° to

the beam and a linear polarizer at 0° to the beam. The effects of elements in the polarimeter are analyzed through use of the Mueller calculus [23]. The Mueller matrix for the PEM (or for any retarder) is given by

$$
\underline{M}_{\mathrm{PEM}} = \begin{bmatrix} 1 & 0 & 0 & 0 \\ 0 & 1-(1-\cos\Delta)\sin^2 2\zeta & \sin 2\zeta\cos 2\zeta(1-\cos\Delta) & -\sin 2\zeta\sin\Delta \\ 0 & \sin 2\zeta\cos 2\zeta(1-\cos\Delta) & 1-(1-\cos\Delta)\cos^2 2\zeta & \cos 2\zeta\sin\Delta \\ 0 & \sin 2\zeta\sin\Delta & -\cos 2\zeta\sin\Delta & \cos\Delta \end{bmatrix} , \tag{2.3}
$$

where Δ is the retardation and ζ the angle between the oscillation axis and the z axis. The matrix for a polarizer at angle θ to the z axis is given by

$$
\underline{M}_{\mathrm{pol}} = \begin{bmatrix} 1 & \cos 2\theta & \sin 2\theta & 0 \\ \cos 2\theta & \cos^2 2\theta & \sin 2\theta\cos 2\theta & 0 \\ \sin 2\theta & \sin 2\theta\cos 2\theta & \sin^2 2\theta & 0 \\ 0 & 0 & 0 & 0 \end{bmatrix} . \tag{2.4}
$$

Taking the Stokes vector for the incident light as

$$
\mathbf{S} = \begin{bmatrix} S_0 \\ S_1 \\ S_2 \\ S_3 \end{bmatrix} , \tag{2.5}
$$

the Stokes vector for the light after the action of the PEM and polarizer is given by

$$
\mathbf{S}' = \underline{M}_{\mathrm{pol}} \cdot \underline{M}_{\mathrm{PEM}} \cdot \mathbf{S} , \tag{2.6}
$$

which yields a rather complicated expression in general. As stated above, though, we set $\zeta = 45°$ and $\theta = 0°$. This allows the total intensity seen after the polarizer to be obtained from the first element of $\mathbf{S}'$ as
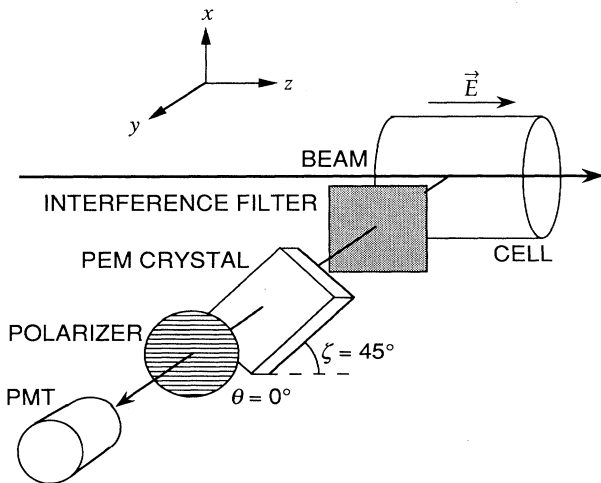
FIG. 2. Schematic of the optical system and polarimeter. Two lenses, not shown, focus light emitted from the H atoms in the collision cell on the PEM.

$$
I = \tfrac{1}{2}(S_0 + S_1\cos\Delta - S_3\sin\Delta) . \tag{2.7}
$$

Recall that $\Delta = \Delta_0\sin\omega t + \delta$. The inherent dc retardation δ of a PEM crystal is made as small as possible by the manufacturer. If we neglect the dc retardation term in the $\cos\Delta$ and $\sin\Delta$ terms, we get an expression for the light intensity as a function of time:

$$
I(t) = \tfrac{1}{2}[S_0 + S_1 J_0(\Delta_0)] + S_1 \sum_{n=1}^{\infty} J_{2n}(\Delta_0)\cos(2n\omega t)
$$
$$
- S_3 \sum_{n=1}^{\infty} J_{2n+1}(\Delta_0)\sin[(2n+1)\omega t] . \tag{2.8}
$$

The retardation is then adjusted to $\Delta_0 = 2.405$ rad. Since $J_0(\Delta_0) = 0$, Eq. (2.8) yields light intensity whose dc component is proportional to S_0 and whose even and odd modulation harmonics are proportional to S_1 and S_3. This can then be decoded via lock-in detection.

The Balmer-α light signal from the H atoms is small enough that photon-counting techniques must be used, yielding count rates on the order of 100–200 Hz. Conventional lock-in amplifiers, used with analog signals, are of little use with photon-counting techniques. Instead, we use an extension of a previously demonstrated [24] device that sends the photon counts through a set of synchronous gates so as to mimic the actions of a lock-in amplifier. This is referred to here as a *digital lock-in* (DLI) device. This has been described elsewhere in some detail [20], so only an overview will be given here.

A schematic of the optical system is shown at the left of Fig. 1. The pulses from a photomultiplier tube (PMT) are sent first to the DLI, whose output goes to five conventional counters: A, B, C, D, and T. The T counter counts continuously during the measurement, while the other four are gated by four transistor-transistor logic (TTL) square waves generated by the DLI according to the scheme shown in Fig. 3. Counts are accepted by each of the four counters when its gate signal is "logic high." The square wave signals for the four gates are synchronous with each other and offset from the reference signal, supplied by the PEM controller, by a phase angle ϕ_0, which we adjust to be as small as possible. The laboratory computer triggers the measurement and records the counts accumulated in all five counters.

The duty cycle of the four gates is not exactly 50%, so a correction is made. Counts are taken, as mentioned above, both with gas in the collision cell and with it rout-
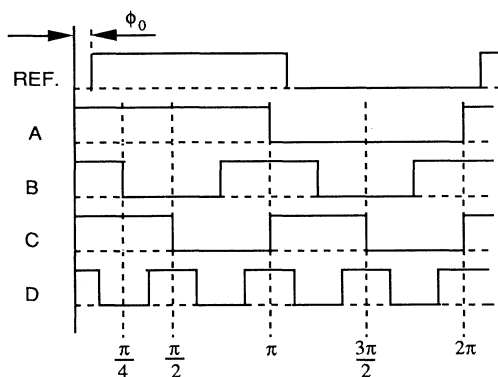
FIG. 3. The gating scheme used by the digital lock-in amplifier, described in the text, in order to decode the modulated light signal presented by the polarimeter. Pulses from the photomultiplier are admitted to the A, B, C, and D counters when the corresponding gate is logic high. A fifth T counter collects counts continuously.

ed to the background region. The difference between gas-in-cell and background counts is normalized to the beam current and to the cell pressure, yielding five signals: I_A, I_B, I_C, I_D, and I_T. The signal I_T corresponds to the normalized intensity from the atoms in the target cell, with background subtracted, integrated over the total count time. The other four signals represent the intensity integrated over the time during which the corresponding gate is open.

Proper combinations of the five signals will yield the desired Stokes parameters. For example, S_1 can be obtained from the B counter and T counter signals by the expression

$$(2I_B - I_T) = S_1 \frac{2}{\pi} \sum_{n=1}^{\infty} \frac{(-1)^n}{2n+1} J_{4n+2}(\Delta_0)\cos(4n+2)\phi_0 .$$

$$(2.9)$$

As stated above, we set the phase angle ϕ_0 as close to zero as possible. Denoting certain useful sums of Bessel functions with

$$\Sigma_o = \frac{2}{\pi} \sum_{n=1}^{\infty} \frac{1}{2n+1} J_{2n+1}(\Delta_0)$$

$$(2.10)$$

and

$$\Sigma_e = \frac{2}{\pi} \sum_{n=1}^{\infty} \frac{(-1)^n}{2n+1} J_{4n+2}(\Delta_0)$$

$$(2.11)$$

(where o and e denote odd and even) and taking $\phi_0 = 0$, we can write

$$S_1 = \frac{1}{\Sigma_e}(2I_B - I_T)$$

$$(2.12)$$

and

$$S_3 = \frac{1}{\Sigma_o}(I_T - 2I_A) .$$

$$(2.13)$$

The intensity S_0 is obtained from the T counter's signal:

$$I_T = \tfrac{1}{2}[S_0 + S_1 J_0(\Delta_0)] .$$

$$(2.14)$$

The sums Σ_o and Σ_e are separately calculated once the retardation of the PEM is known. The procedure for calibrating the PEM retardation has been described by Cline, Westerveld, and Risley [20]. With the PEM and polarizer aligned as described, it is not possible to determine S_2, but from symmetry arguments S_2 is required to be zero when the H atom is in an axial field. We could measure S_2, if desired, by setting the PEM at $\zeta = 0°$ and the polarizer at $\theta = 45°$, but we elected here not to do so.

For the data presented here, the retardation is $\Delta_0 = 2.405 \pm 0.005$ rad. The phase offset is $\phi_0 = 0.38° \pm 0.02°$.

2. Corrections for imperfections

In the analysis above, we assume that the PEM and polarizer are perfectly aligned with the beam, at $\zeta = 45°$ and $\theta = 0°$, respectively, and also that the inherent retardation δ of the PEM crystal is negligible. These assumptions can contribute systematic errors.

The effect of a nonzero δ is to mix the Stokes parameters. It can be shown that if δ is included in the analysis, the Stokes parameters found are replaced by "effective" Stokes parameters, given by

$$S_1^{\text{eff}} = S_1\cos\delta - S_3\sin\delta ,$$
$$S_3^{\text{eff}} = S_3\cos\delta + S_1\sin\delta .$$

$$(2.15)$$

Fortuitously, in the experiment, symmetry in the collision in an axial field requires that $S_3 = 0$. Any nonzero S_3^{eff} observed must be then due to a nonzero retardation δ, the effect of which will also be to artificially reduce S_1. We use this information to determine this retardation as

$$\delta = \tan^{-1}\left[\frac{S_3^{\text{eff}}}{S_1^{\text{eff}}}\right].$$

$$(2.16)$$

The value found is then used to correct the observed value of S_1. We have found the retardation of the present crystal to be $\delta = 0.01 \pm 0.04$ rad, which produces a very small correction.

Imperfect alignment of the PEM and polarizer also induces a systematic error. It can be shown that the effective Stokes parameters in the general case (now neglecting again effects due to nonzero δ) are given by

$$S_0^{\text{eff}} = S_0 ,$$

$$(2.17)$$

$$S_1^{\text{eff}} = S_1\sin^2 2\zeta \cos 2\theta ,$$

$$(2.18)$$

$$S_3^{\text{eff}} = S_3\sin 2\zeta \cos 2\theta .$$

$$(2.19)$$

The effective values tend to the real values as ζ approaches 45° and θ approaches 0°. To align the system, the PEM and polarizer were first mechanically aligned with each other to $\pm 0.5°$. Polarized light from a He target collision was then observed and the polarizer rotated to maximize S_1^{eff}. Idiosyncrasies of the mount prevented similar rotation and checking of the PEM, but since the PEM and polarizer were initially well aligned to each other, the PEM was simply rotated to match the polariz-

er. We estimate that this procedure left the system aligned to $\pm 1°$. Such a misalignment will induce negligible errors in the Stokes parameters and density-matrix elements.

Models of PEM behavior taking additional effects into account are available. Acher, Bigan, and Drévillon [25] have pointed out that Eq. (2.2) does not include all possible static retardation effects and have described a model including higher harmonic modulation terms. The effect of a static retardation along axes not parallel to the modulation axis has been treated by Badoz, Silverman, and Canit [26] and by Modine and Jellison [27]. Since, however, our PEM polarimeter has produced results equivalent to our earlier experiments, which used a different polarimeter, we neglect these other effects.

3. Normalization and error analysis

The procedure described above will determine three of the four Stokes parameters in arbitrary units. The data presented here, though, are normalized to the value of S_0 at zero electric field.

For proper analysis of errors in the density-matrix elements, it is necessary to know the covariance matrix for the three measured Stokes parameters. A covariance matrix for the five signals I_A, I_B, I_C, I_D, and I_T can be calculated, but determination of a covariance matrix for the Stokes parameters from it is complicated as the five quantities are not statistically independent. A simpler approach was devised by Cline [28], in which one period of oscillation of the PEM crystal is divided into 16 segments. During each segment, the five quantities are statistically independent. A Jacobean transform is then performed to obtain a 3×3 covariance matrix for the Stokes parameters from the diagonal 16×16 matrix for the independent quantities. All covariances in the Stokes parameters' matrix are then dependent on σ_T^2, the statistical counting error in the signal I_T from the T counter.

This is not quite sufficient, as additional random errors are present in the experiment. In order to account for this, measured variation in $S_0(E=0)$, which is determined for normalization purposes. is used to empirically adjust σ_T^2. Additional errors resulting from the normalization are then factored in. This results in an error-bar determination for the Stokes parameters that includes all known sources of random error.

III. DATA COLLECTION AND ANALYSIS

A. General

Data are presented for 25–100-keV protons on He, for comparison with earlier results, and for 20–100-keV protons on Ar. The Ar target requires additional corrections to the Stokes parameters, which are described in Sec. III B.

A microcomputer is used to automate data collection. The five signals I_A, I_B, I_C, I_D, and I_T are measured at positive and negative values of 18 different standard values of the axial electric field E, plus $E=0$, for a total of 37 different fields. The transverse field was not used in this study for reasons which are given in Sec. III C. The

standard values are applied in random order by the computer with a custom programmable power supply. Measurement at each value of E is followed by a measurement at $E=0$ for normalization. Typical count rates with gas in the cell are 100–200 Hz, and typical count times are on the order of 5–10 min. Background subtraction is automatically performed as described in Sec. II A. A complete set of data at all 37 values of electric field generally requires 12–16 h of collection time, although longer times are used at the lower beam energies, where beam currents are lower.

After data collection is completed, the microcomputer is used to analyze the raw data by the method described in Sec. II to obtain the Stokes parameters. Typical errors are about $\pm 1\%$ for S_0, $\pm 5\%$ for S_1, and ± 50–100% for S_3. Recall that the measured value of S_3 is nearly zero. S_0 and S_1 are corrected for the systematic effects described previously and then fit to the calculated H atom model, as described in Sec. III C, in order to extract density matrix elements.

A sample set of Stokes data, for 60-keV protons on Ar, is shown in Fig. 4. The qualitative features can be explained as follows: We see that the unpolarized intensity S_0 increases with electric field. This is due to Stark mixing of the s, p, and d states as the external field is increased. The structure in the curve and its rate of increase contain information about the relative populations of those states. The initial swift increase at low fields is due to p-d mixing, where the intensity goes up as the p population is mixed with the d, suppressing the p population decay via Lyman-β radiation. At high electric fields, the field allows the slowly decaying s state to decay by mixing with the other, more swiftly decaying states, so the light intensity increases still more [29].

Similar information is available from S_1: since each decaying state will have a characteristic linear polarization fraction [30], the polarization observed will change as the states are mixed by the field. The use of both S_0 and S_1 data allows us to determine state populations with high precision. Also visible is a spurious nonzero S_3, the effect to which we referred in Sec. II as being due to polarimeter imperfection.

Finally, we clearly see an asymmetry between positive-field and negative-field values of S_0 and S_1. This asymmetry, showing that the H atom is sensitive to the direction as well as the strength of the electric field, clearly indicates that the H atom produced in the collision possesses an electric dipole moment.

B. Special considerations for the Ar target

Light from the collision is observed through a standard interference filter, with a manufacturer-specified bandpass of 10.0 nm centered at 656.2 nm. While the He atom possesses no transition lines within this range, the Ar atom has five lines [31,32], at 649.4, 660.4, 660.5, 653.8, and 659.6 nm, resulting from transitions from the $4d'$ manifold to the $4p$ manifold, that are visible through this filter. Two $7s$ to $4p$ transitions, at 651.4 and 659.9 nm, are also visible. A partial level diagram is shown in Fig. 5. Since Ar atoms excited by proton impact decay in

the detector's field of view, light from these transitions can present a serious signal contamination problem. A procedure was devised for estimating the amount of the signal contributed by Ar atoms.

We wish to calculate the ratio F of Ar-emitted light intensity seen through the 656.2-nm filter to Balmer-α light intensity:

$$F = \frac{S_0^{(Ar)}}{S_0^{(H)}} \ . \tag{3.1}$$

Knowledge of photoemission cross sections for these transitions, combined with our system detection efficiency, would make the task simple. These cross sections are, however, unavailable. One of the advantages of the PEM polarimeter is that we can accurately measure Stokes parameters at any wavelength simply by adjusting the PEM retardation. We can estimate F by using another filter, centered at 690.0 nm, to measure the intensity of other transitions from the same $4d'$ level. We can use the ratio of the observed intensities to calculate F. Eight Ar
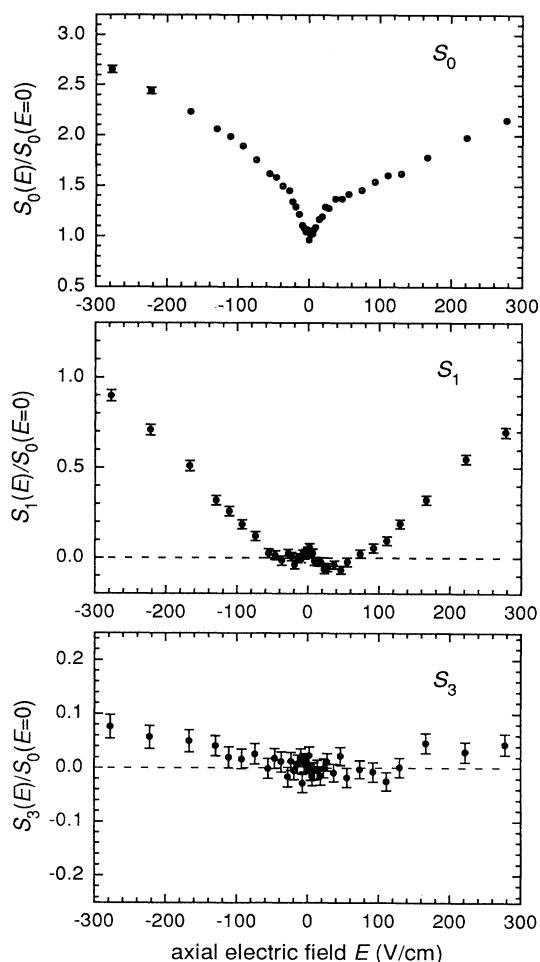

FIG. 4. Sample Stokes data, emitted by Balmer-α decay of H($n = 3$) atoms produced by 60-keV collisions of protons with Ar. All Stokes parameters are normalized to the value of S_0 at zero electric field.
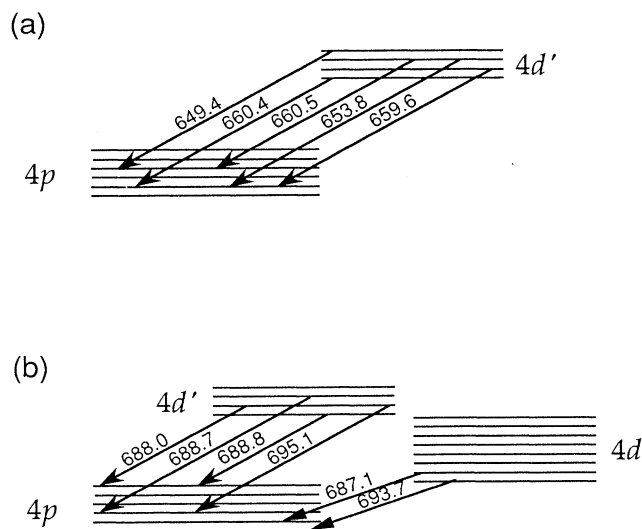

FIG. 5. A partial level scheme for the Ar atom: (a) shows the most important transition lines that contaminate the Balmer-α signal from H atoms and (b) shows the lines visible through the 690-nm filter used in a calibration procedure described in Sec. III B.

lines are visible through the 690-nm filter: 688.0, 688.7, 688.8, and 695.1 nm from $4d'$ to $4p$ transitions; 687.1 and 693.7 nm from $4d$ to $4p$ transitions; and 685.1 and 690.5 nm from $5d$ to $4p'$ transitions.

Both S_0 and S_1 were measured with the 690-nm filter, but S_1 was found to be indistinguishable from zero. As this was expected, it was assumed that S_1 was also zero for the Ar light visible through the 656.2-nm filter. It was also found, as expected, that the intensity S_0 observed with the 690-nm filter did not change with electric field. The field may well mix Ar states, but, as all Ar decays are observed, no matter how long the lifetime is, the brightness of the light will not change. The correction, then, is essentially one of normalization, as all our data are normalized to $S_0(E = 0)$. We obtain the correction factor F from zero-field measurements of S_0, as follows.

The intensity of light seen from the excited Ar atoms is directly related to the photoemission cross sections $\sigma_{pe}(\lambda)$ for the lines observed. Since we can see seven transition lines through the 656.2-nm filter, we write

$$S_0^{(Ar)} = k \sum_{i=1}^{7} \sigma_{pe}(\lambda_i) \ , \tag{3.2}$$

where the factor k includes proportionality factors for beam current, cell pressure, and detection system efficiency. The efficiency of the filter-photomultiplier combination is assumed constant for all wavelengths visible with the filter. By replacing k with a k', we write a similar equation for intensity of Ar lines seen through the 690-nm filter as

$$S_0^{'(Ar)} = k' \sum_{j=1}^{8} \sigma_{pe}(\lambda_j) \ , \tag{3.3}$$

where we again assume constant efficiency over the wave-

lengths within the bandpass of the filter. If experimental conditions remain constant, the only parameter distinguishing k from k' will be the spectral response of our photomultiplier.

As most of the observed decays originate in the same manifold, the $4d'$, it is useful to write the intensities in terms of cross sections for excitation to this level. We can write the following relation between excitation cross sections σ_{ex} and photoemission cross sections σ_{pe}:

$$\sigma_{pe}(\lambda_i) = \sigma_{ex}\frac{W_i}{N} , \qquad (3.4)$$

where W_i is the branching ratio of the transition with wavelength λ_i and N is the number of fine-structure sublevels of the nl manifold excited (e.g., the $4d'$ manifold has $N = 4$ sublevels). We neglect cascade effects and assume that all sublevels are excited with equal probability. To apply this to the problem at hand, we make the additional assumptions that

$$\sigma_{ex}(4d) = \sigma_{ex}(4d') , \qquad (3.5)$$

$$\sigma_{ex}(n) = \left[\frac{4}{n}\right]^3 \sigma_{ex}(4d') , \qquad (3.6)$$

where Eq. (3.6) uses the $1/n^3$ scaling law to estimate excitation to higher levels. Although the $1/n^3$ scaling law may not be accurate, significant deviations from it would not affect the final conclusion. This allows us to write the two intensities as

$$S_0^{(Ar)} = k\sigma_{ex}(4d') \left[\frac{1}{4}\sum_{i=1}^{5} W_i + (\frac{4}{7})^3\frac{1}{2}\sum_{i=6}^{7} W_i\right] , \qquad (3.7)$$

$$S_0'^{(Ar)} = k'\sigma_{ex}(4d') \left[\frac{1}{4}\sum_{j=1}^{4} W_j + \frac{1}{8}\sum_{j=5}^{6} W_j + (\frac{4}{5})^3\frac{1}{4}\sum_{j=7}^{8} W_j\right] , \qquad (3.8)$$

where in Eq. (3.7) transitions from the $4d'$ manifold are numbered (arbitrarily) 1 through 5 and transitions from the $7s$ level are numbered 6 and 7. In Eq. (3.8) the first term refers to transitions from the $4d'$ manifold, the second to those from $4d$, and the third to those from $5d$.

Branching ratios for the transitions of interest were calculated from transition rates available in the compilation by Wiese, Smith, and Miles [32]. Using these numbers (many of which are known only to $\pm50\%$) and including the manufacturer's specified spectral response for our photomultiplier yields the ratio for the Ar light intensities visible through the two filters as

$$\frac{S_0^{(Ar)}}{S_0'^{(Ar)}} = 0.38\pm0.35 . \qquad (3.9)$$

This number is then used in conjunction with measured light intensities through the two filters to obtain the ratio F, defined in Eq. (3.1). This ratio ranges from a minimum of $F = 0.04$ at 20 keV to a maximum of $F = 0.29$ at 100 keV, and is given as a function of beam energy in Table I. As will be seen below, the large uncertainty here has little effect on the final density-matrix results.

TABLE I. The ratio F of light intensity emitted by excited Ar-target atoms through the 656.2-nm filter to that of Balmer-α light emitted by the excited H atoms. This ratio was obtained as described in Sec. III B.

Beam energy (keV)	F	Min. F	Max. F
20	0.04	0.002	0.07
25	0.04	0.003	0.08
30	0.05	0.003	0.11
35	0.06	0.004	0.12
40	0.07	0.004	0.14
50	0.09	0.005	0.18
60	0.11	0.007	0.24
80	0.17	0.010	0.40
100	0.29	0.015	0.78

The ratio F is then used to correct the data as follows. We necessarily observe intensity from both H and Ar atoms, yielding at nonzero electric field E the expression

$$S_0^{(tot)}(E) = S_0^{(H)} + S_0^{(Ar)} , \qquad (3.10)$$

as the intensity from Ar atoms does not change with electric field. We also measure the intensity at zero electric field for normalization, which is

$$S_0^{(tot)}(E=0) = S_0^{(H)}(E=0) + S_0^{(Ar)}(E=0)$$
$$= (1+F)S_0^{(H)}(E=0) . \qquad (3.11)$$

This information is used to obtain the desired normalized intensity from H atoms, which is given by

$$\frac{S_0^{(H)}(E)}{S_0^{(H)}(E=0)} = (1+F)\frac{S_0^{(tot)}(E)}{S_0^{(tot)}(E=0)} - F . \qquad (3.12)$$

The correction for S_1 is only one of normalization:

$$\frac{S_1^{(H)}(E)}{S_0^{(H)}(E=0)} = (1+F)\frac{S_1^{(tot)}(E)}{S_0^{(tot)}(E=0)} . \qquad (3.13)$$

The corrections are applied to the Stokes data before the data are fit. At 100 keV, for example, the correction of $F = 0.29$ results in an 18% change in intensity at the highest electric fields used. The effect of this correction is small and will be discussed in Sec. IV.

C. Use of fitting functions: Determining the density matrix

The procedure for analyzing the Stokes-parameter data has been described in detail previously [2], so we will give only a brief description here. The light observed is emitted from H($n = 3$) atoms formed all along the beam in the collision region and coherently excited into a linear superposition of substates with $n = 3$, which will decay as they proceed down the beam line through the target cell. This superposition of states formed at the instant of capture is best described by a 36×36 density matrix $\underline{\sigma}_3$. This matrix can be obtained by an analysis method that takes into account contributions to the Stokes parameters from all the different states and accounts for their time

evolution as they proceed through the apparatus. Diagonal elements of $\underline{\sigma}_3$ are the cross sections for capture to the various substates, while off-diagonal elements represent coherences of the capture process between the different eigenstates, averaged over all impact parameters and azimuthal angles.

This large matrix can be simplified. As the time scales for the collision are much shorter than characteristic time scales for the excited atoms' internal dynamics, the charge-transfer process and the subsequent time evolution can be cleanly separated. This is why the results of our experiment, concerning capture in an external field, can be applied to the general zero-field capture process. As the spins of the electron and proton do not affect the capture process, we can neglect their influence in the density matrix and reduce the 36×36 matrix $\underline{\sigma}_3$ to a more manageable 9×9 matrix $\underline{\sigma}_L$. Finally, since our experiment is cylindrically symmetric, the lack of dependence on azimuthal angle removes many of the 81 elements of $\underline{\sigma}_L$: coherence terms between states of different m_l are zero and the matrix elements depend only on $|m_l|$. The density matrix is also Hermitian.

As a result of these symmetries, only 14 independent parameters are necessary to completely determine this matrix. We separately measure the real and imaginary parts of the coherence terms. This leads to six diagonal elements, denoted σ_{s0}, σ_{p0}, $\sigma_{p\pm1}$, σ_{d0}, $\sigma_{d\pm1}$, and $\sigma_{d\pm2}$, and eight coherence elements $\mathrm{Re}(\sigma_{s0p0})$, $\mathrm{Im}(\sigma_{s0p0})$, $\mathrm{Re}(\sigma_{s0d0})$, $\mathrm{Im}(\sigma_{s0d0})$, $\mathrm{Re}(\sigma_{p0d0})$, $\mathrm{Im}(\sigma_{p0d0})$, $\mathrm{Re}(\sigma_{p\pm1d\pm1})$, and $\mathrm{Im}(\sigma_{p\pm1d\pm1})$. In addition to the matrix elements themselves, we obtain the dipole moment $d=\langle\mathbf{d}\rangle_z$ of the H atom immediately following the collision.

For a given density matrix, the intensity and polarization—the Stokes parameters—of the emitted light due to each of the matrix elements can be calculated from first principles. We use a numerical program to perform this calculation, which takes into account the time evolution of H atoms in our own particular experimental apparatus, including such effects as an accurate model of the electric field, the viewing region of the polarimeter, and the target number density as a function of z. Neglecting cascade, the measured Stokes parameters can be written as a sum of contributions from each of the density-matrix elements:

$$S_i(E)=\sum_{j,k}f_{ijk}(E)\sigma_{jk}\ ,\qquad(3.14)$$

where i is the Stokes-parameter index and j and k are the angular-momentum indices for the density-matrix element σ_{jk}. The quantity f_{ijk} represents the optical contribution to Stokes parameter S_i from density-matrix element σ_{jk} and is referred to as a "fitting function." These fitting functions are calculated by the computer program. A linear statistical fit of the Stokes data to the fitting functions, in the form given by Eq. (3.14), yields the desired density-matrix elements.

Cascade from the $n=4$ state is accounted for by use of another set of fitting functions g_{ijk}, calculated by a somewhat simplified procedure, and the two are combined for use in the fitting procedure [2].

In previous work, data were collected using both an axial and a transverse field. This required use of *two* sets of fitting functions, $f_{ijk}^{(a)}$ for the axial-field measurements and $f_{ijk}^{(t)}$ for the transverse field. Both are required in order to measure precisely all the density-matrix elements. In this work, only an axial field was used, for reasons which are discussed in Sec. IV A.

Standard linear fitting methods [33,34], that include correlation between the Stokes parameters are used. We rewrite Eq. (3.14) in matrix form as

$$\mathbf{S}^{\mathrm{fit}}=\underline{F}\cdot\sigma^{\mathrm{col}}\ ,\qquad(3.15)$$

where $\mathbf{S}^{\mathrm{fit}}$ is a column vector containing the fitted values for all the Stokes parameters, $\underline{F}$ is a matrix composed of all the fitting functions, and σ^{col} is a vector containing the desired density-matrix elements. This fit is good when the quantity χ^2 is minimized. We define a weighting matrix $\underline{W}$ as the inverse of the covariance matrix $\underline{C}_b$ for the Stokes parameters:

$$\underline{W}=\underline{C}_b^{-1}\ .\qquad(3.16)$$

The weighted linear fit obtains the density-matrix elements in the vector σ^{col} from the measured Stokes parameters in a vector $\mathbf{S}^{\mathrm{meas}}$. In this fit, χ^2 is minimized when

$$\sigma^{\mathrm{col}}=(\underline{F}^{\mathrm{T}}\cdot\underline{W}\cdot\underline{F})^{-1}\cdot\underline{F}^{\mathrm{T}}\cdot\underline{W}\cdot\mathbf{S}^{\mathrm{meas}}\ .\qquad(3.17)$$

The covariance matrix for the density-matrix elements is given by

$$\underline{C}_\sigma=(\underline{F}^{\mathrm{T}}\cdot\underline{W}\cdot\underline{F})^{-1}\ .\qquad(3.18)$$

Density-matrix elements presented in Sec. IV are determined by the above procedure using the same fitting functions as used previously [2,3]. As the fitting function does not depend on the target, the same functions are used for the He and Ar targets.

IV. RESULTS AND DISCUSSION

A. Use of axial and transverse fields and the resulting density matrix

The elements of the density matrix yield important physical parameters of the collision and its resulting H atom. The diagonal elements (σ_{s0}, σ_{p0}, $\sigma_{p\pm1}$, etc.) are partial cross sections for capture to their corresponding angular-momentum substates of $n=3$. The meaning of the off-diagonal coherence terms can be found by calculating the expectation value of certain quantum-mechanical operators [18]. For example, several of the real parts of the coherence terms are used to find the expectation value of the first moment of the electron-density distribution, or the atom's electric dipole moment:

$$\langle\mathbf{d}\rangle_z=\frac{ea_0}{\mathrm{Tr}(\underline{\sigma}_L)}[6\sqrt{6}\,\mathrm{Re}(\sigma_{s0p0})+6\sqrt{3}\,\mathrm{Re}(\sigma_{p0d0})$$
$$+18\,\mathrm{Re}(\sigma_{p\pm1d\pm1})]\ .\qquad(4.1)$$

The imaginary parts of the coherence terms are used to calculate parameters of the atom's current distribution $\mathbf{j}(\mathbf{r})$. For example, a nonzero first moment of the distribution is given by

$$\langle \mathbf{L} \times \mathbf{A} \rangle_{z,s} = \frac{-4\hbar^2}{\mathrm{Tr}(\underline{\sigma}_L)} (\tfrac{2}{3})^{1/2} [\mathrm{Im}(\sigma_{s0p0}) + \sqrt{2}\,\mathrm{Im}(\sigma_{p0d0})$$

$$+ \sqrt{6}\,\mathrm{Im}(\sigma_{p\pm1\,d\pm1})] \ . \qquad (4.2)$$

To determine precisely all the density-matrix elements, it is necessary to use both the axial and the transverse fields in the experiment, as some elements make a much stronger contribution to the Stokes parameters in one orientation. For example, examination of the fitting functions reveals that the contribution from the $\mathrm{Im}(\sigma_{s0p0})$ term to S_0 and S_1 in the axial field is some three orders of magnitude less than the prominent contributions from the $\mathrm{Re}(\sigma_{s0p0})$ or the $\sigma_{p\pm1}$ elements. Thus, unless conditions of the collision are such that the $\mathrm{Im}(\sigma_{s0p0})$ term is produced with very high probability, the axial field will yield a poor measurement of this term. With the transverse field, it is seen that $\mathrm{Im}(\sigma_{s0p0})$ makes no contribution at all to S_0 and S_1 but contributes strongly to S_2 and S_3. Thus the transverse field is necessary to measure this imaginary coherence term. This has been found to be true in general for imaginary parts of the coherence terms, while real parts are, on the other hand, easier to measure with the axial field [3]. A physical description of this effect, while desirable, is elusive.

The primary motive for the present work was to measure the dipole moment of the H atoms, an important physical parameter of the collision, and compare results from the two different targets. The dipole moment depends, as shown in Eq. (4.1), on real parts of coherence terms, which are more precisely determined with an axial field. This is also true of the desired diagonal p elements.

In earlier work it was found that the diagonal s and d elements were better determined with a transverse field, but as the s term is generally the largest one, the axial-field measurement yields acceptable precision. The d elements are the smallest and hence are difficult to find in any case. Thus, we use only an axial field for the present work.

B. Helium target results

As a test of the PEM system, we took measurements of the density matrix for $\mathrm{H}(n=3)$ atoms produced by 25–100-keV protons colliding with He for comparison with earlier results. Table II shows matrix elements and the dipole moment for a 40-keV He target collision. Results from previous work from the axial field alone and from axial and transverse fields analyzed in combinations are shown for comparison. The collisionally produced $\mathrm{H}(n=3)$ dipole moment for the He target for all energies is shown in Fig. 6. Quite good agreement is seen between matrix elements and between dipole moments obtained using the two different polarimeters, although the uncertainties are significantly higher for the new results. This effect occurs for two reasons. In the earlier work, the experiment was run for significantly longer times (about one week per beam energy versus one day per beam energy for the present results), improving the counting statistics. Moreover, the error bars for the present results include, as described in Sec. II C, random errors in addition to those from statistical counting errors. Thus the error bars for the present results would be somewhat larger than in the previous work even if the same counting time were used. When data are collected for the same length of time as previously and errors are analyzed in the same way, the results are comparable, indicating that the PEM itself induces no additional random error. We thus conclude that the PEM polarimeter is as accurate and precise as the rotating-retarder polarimeter used earlier.

TABLE II. Density-matrix elements and the electric dipole moment for $\mathrm{H}(n=3)$ produced from 40-keV protons on He. The present results are compared to results from Ref. [3], which used the same apparatus with a different polarimeter. Results from the previous work are shown from measurements with an axial field in the collision cell and from a combined fit to both axial and transverse measurements. The present results used only the axial field and shorter measurement times.

| Matrix element	Ref. [3], axial	Ref. [3], combined	Present results
σ_{s0}	1.000 ± 0.017	1.000 ± 0.008	1.00 ± 0.07
σ_{p0}	0.415 ± 0.012	0.417 ± 0.005	0.43 ± 0.04
$\sigma_{p\pm1}$	0.051 ± 0.005	0.034 ± 0.003	0.08 ± 0.02
σ_{d0}	0.04 ± 0.02	0.051 ± 0.006	0.07 ± 0.09
$\sigma_{d\pm1}$	0.008 ± 0.017	-0.003 ± 0.005	-0.01 ± 0.06
$\sigma_{d\pm2}$	0.006 ± 0.005	0.012 ± 0.001	0.009 ± 0.016
$\mathrm{Re}(\sigma_{s0p0})$	0.416 ± 0.011	0.397 ± 0.007	0.41 ± 0.04
$\mathrm{Im}(\sigma_{s0p0})$	-1.6 ± 0.8	-0.247 ± 0.007	-2.6 ± 3.0
$\mathrm{Re}(\sigma_{s0d0})$	0.10 ± 0.03	0.129 ± 0.008	0.11 ± 0.10
$\mathrm{Im}(\sigma_{s0d0})$	-0.11 ± 0.11	-0.14 ± 0.03	-0.5 ± 0.4
$\mathrm{Re}(\sigma_{p0d0})$	0.099 ± 0.005	0.097 ± 0.003	0.112 ± 0.019
$\mathrm{Im}(\sigma_{p0d0})$	0.020 ± 0.005	0.22 ± 0.002	0.026 ± 0.016
$\mathrm{Re}(\sigma_{p\pm1\,d\pm1})$	0.011 ± 0.006	0.017 ± 0.004	0.00 ± 0.03
$\mathrm{Im}(\sigma_{p\pm1\,d\pm1})$	0.008 ± 0.007	0.006 ± 0.001	0.03 ± 0.02
$\langle d \rangle_z$	4.65 ± 0.07	4.57 ± 0.06	4.41 ± 0.26
χ^2	1.30	1.11	0.85
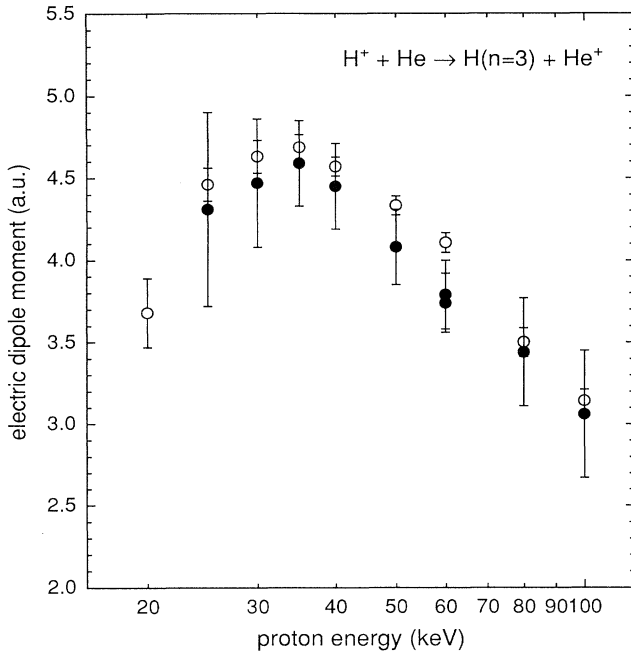
FIG. 6. The dipole moment for H($n=3$) atoms produced from electron capture from He. ●, present results with the new polarimeter; ○, results from previous work with a different polarimeter (Ref. [3]) presented for comparison. The error bars in the present work include random errors not included in Ref. [3].

after analysis with and without the $F=0.29$ correction. While differences in the measured density-matrix elements and dipole moments are visible, the difference is well within experimental errors for this worst case.

This is shown graphically in Fig. 7, where corrected and uncorrected data are shown together. Sums of normalized fitting functions, weighted by their contributions to the corrected data, are also shown. As the correction preserves the structure in the data, we see that the apparent intensity shift caused by the correction must be spread among the fitting functions, causing only small changes in their relative weights. Thus the density-matrix elements, which are all normalized to the σ_{s0} element, suffer little change.

Density-matrix elements obtained from corrected data are shown in Table IV. As the imaginary parts of the coherence terms are determined so weakly with the axial-field setup (as seen in Table II), only the real parts are presented. The s and p diagonal elements are obtained with good precision, with errors ranging from $\pm3\%$ to $\pm13\%$ for the s element and $\pm5\%$ to $\pm22\%$ for the p elements. The d elements are not only rather small, but, as noted previously, better determined with a transverse field. Figure 7 shows that they make only a small contribution to the total intensity in the axial field at a collision energy of 100 keV. The σ_{d0} and $\sigma_{d\pm2}$ elements are, then, poorly determined in the present work. Uncertainties are comparable to the measurements, and some of the elements are less than zero, which is nonphysical.
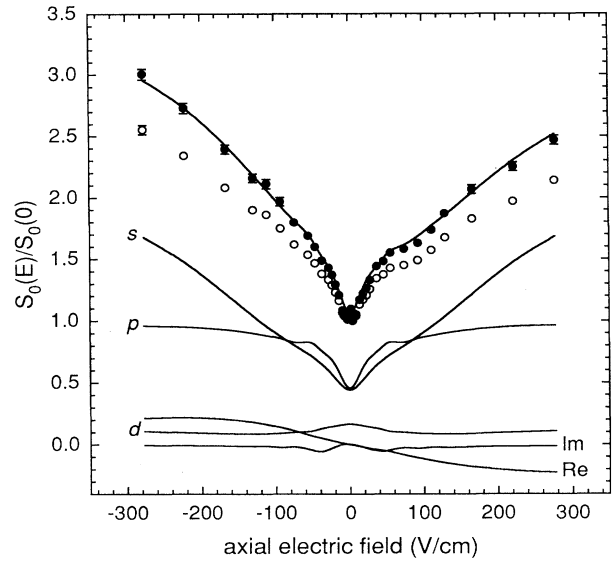
C. Argon-target results

1. Density-matrix elements and dipole moment

Unlike the He target data, the Ar-target Stokes data required the correction for Ar background light described earlier. The reader will note from Table I that the uncertainty in the amount of light emitted by the Ar atoms is large. We investigate the effect of this uncertainty by analyzing the data both with and without the correction. An example of this is shown in Table III, where 100-keV density-matrix elements are presented

TABLE III. Diagonal and real off-diagonal coherence elements for the density matrix for H($n=3$) atoms produced from 100-keV protons on Ar, analyzed with and without accounting for the estimated Ar-light-emission contamination.

Parameter	With correction	Without correction
σ_{s0}	1.00 ± 0.06	1.00 ± 0.06
σ_{p0}	0.21 ± 0.04	0.22 ± 0.04
$\sigma_{p\pm1}$	0.129 ± 0.017	0.142 ± 0.017
σ_{d0}	0.10 ± 0.09	0.10 ± 0.09
$\sigma_{d\pm1}$	-0.05 ± 0.06	-0.04 ± 0.06
$\sigma_{d\pm2}$	0.021 ± 0.016	0.033 ± 0.016
$\mathrm{Re}(\sigma_{s0p0})$	0.10 ± 0.03	0.10 ± 0.03
$\mathrm{Re}(\sigma_{s0d0})$	0.04 ± 0.09	0.04 ± 0.09
$\mathrm{Re}(\sigma_{p0d0})$	-0.001 ± 0.015	-0.001 ± 0.015
$\mathrm{Re}(\sigma_{p\pm1d\pm1})$	0.041 ± 0.018	0.041 ± 0.018
$\langle\mathbf{d}\rangle_z$	1.49 ± 0.20	1.37 ± 0.18
χ^2	1.06	1.05

FIG. 7. The effect of the background-light correction as described in the text. ●, S_0 data for a 100-keV collision with the correction; ○, the same data without the correction. The contribution to S_0 from the fitting functions is shown by the solid lines as follows: s, contribution from σ_{s0}; p, contribution from σ_{p0} and $\sigma_{p\pm1}$; d, contribution from σ_{d0}, $\sigma_{d\pm1}$, and $\sigma_{d\pm2}$; Re, summed contributions from the four real coherence terms; Im, summed contributions from the four imaginary coherence terms. The five individual curves add to give the solid line through the corrected data.

These elements are presented only for completeness. The $\sigma_{d\pm1}$ element is poorly determined at high beam energies but apparently is large enough to be measured with increasing precision at beam energies below 35 keV.

Real parts of coherence terms are generally found with acceptable precision, with the best results obtained for p-d terms. The s-d coherence is rather poorly determined, but is, as noted in Ref. [3], the hardest one to measure. Note that it does not contribute to the dipole moment of the H atom.

The 25-, 35-, and 80-keV data runs were performed twice and the 50-keV run three times. Reproducibility of the matrix elements and dipole moment within quoted error bars is very good. In the fitting of Stokes data described in Sec. III C, χ^2 is calculated as a check of goodness of fit. The average χ^2 was 0.69, with minimum $\chi^2=0.25$ and maximum $\chi^2=1$, indicating that the errors on the present results are properly determined.

These results yield a measurement of the H-atom dipole moment with a precision of $\pm5\%$ to $\pm14\%$, which is more than sufficient to compare to the He target and sufficient for comparison with theory. The collisionally produced dipole moment is shown as a function of energy in Fig. 8, where it is compared with the results for the He target. We see that the dipole produced from an Ar target is consistently smaller than that from a He target. At energies above 50 keV, the data suggest a scaling relationship between dipole moments from the two targets. The H-atom dipoles produced from He and Ar targets are in the ratio 2.1 ± 0.2 (in fact, this ratio persists down to 30 keV). Probability density plots, discussed below, shed light on this behavior.

2. Capture cross sections

If the value of $S_0(E=0)$ is *not* set equal to unity, the fitting procedure yields density-matrix elements (before normalization to σ_{s0s0}) in arbitrary but consistent units. Cross sections for capture to the 3s, 3p, and 3d levels are then placed on an absolute scale by normalization at one energy to other groups' experimental results. This was previously done for the He target by Cline, Westerveld, and Risley [19], where relative He-target capture cross sections were normalized at 60 keV to the absolute results of Brower and Pipkin [17].

Cross sections for capture from the Ar target are shown in Table V. Relative cross sections were obtained by the procedure outlined above. Results from the He target and the Ar target measured with the current apparatus are placed on the same scale by using the Baratron capacitance manometer to calibrate the ion gauge used in both measurements. Current He-target results are again normalized to Brower and Pipkin's measurement at 60 keV. This then also places the Ar-target results on an absolute scale. Errors shown in Table V reflect random uncertainties only, where correlations between the density-matrix elements are taken into account in calculating the error. The 3s cross section is found to a precision of 3–14%. The 3p cross section is found to similar precision, while 3d cross sections are poorly determined, with errors from 30% to well over 100%.

TABLE IV. Diagonal and real off-diagonal coherence terms of the density matrix $\underline{\sigma}_L$, described in the text, for H($n=3$) atoms produced in electron capture from Ar. The electric dipole moment of the H atom is also given in atomic units. All matrix elements have been normalized to the σ_{s0} term. The error bars indicate random errors only.

|	20 keV	25 keV	30 keV	35 keV	40 keV	50 keV	60 keV	80 keV	100 keV
σ_{s0}	1.00±0.13	1.00±0.09	1.00±0.07	1.00±0.05	1.00±0.07	1.00±0.03	1.00±0.06	1.00±0.03	1.00±0.06
σ_{p0}	0.36±0.08	0.34±0.06	0.23±0.04	0.26±0.03	0.30±0.04	0.24±0.02	0.25±0.04	0.16±0.02	0.21±0.04
$\sigma_{p\pm1}$	0.69±0.05	0.50±0.03	0.30±0.02	0.316±0.016	0.28±0.02	0.215±0.010	0.178±0.016	0.112±0.008	0.129±0.017
σ_{d0}	-0.16±0.17	-0.04±0.12	-0.12±0.09	-0.01±0.07	0.03±0.09	0.04±0.05	0.07±0.08	0.04±0.04	0.10±0.09
$\sigma_{d\pm1}$	0.41±0.12	0.20±0.08	0.19±0.06	0.09±0.05	0.04±0.06	0.02±0.03	-0.02±0.06	-0.01±0.03	-0.05±0.06
$\sigma_{d\pm2}$	-0.02±0.03	0.003±0.022	-0.008±0.017	0.007±0.012	0.016±0.016	0.015±0.008	0.021±0.014	0.015±0.008	0.021±0.016
Re(σ_{s0p0})	0.05±0.12	0.05±0.07	0.14±0.05	0.11±0.03	0.17±0.04	0.162±0.019	0.20±0.03	0.148±0.016	0.10±0.03
Re(σ_{s0d0})	-0.24±0.22	-0.09±0.15	-0.16±0.11	-0.03±0.08	-0.01±0.11	0.03±0.05	0.05±0.09	0.04±0.04	0.04±0.09
Re(σ_{p0d0})	0.13±0.06	0.12±0.03	0.12±0.02	0.075±0.013	0.049±0.017	0.049±0.008	0.034±0.014	-0.01±0.03	-0.001±0.015
Re($\sigma_{p\pm1d\pm1}$)	0.30±0.07	0.20±0.04	0.07±0.03	0.085±0.018	0.08±0.02	0.035±0.011	0.019±0.018	0.015±0.008	0.041±0.018
$\langle d \rangle_z$	2.22±0.32	2.03±0.23	2.17±0.21	1.92±0.14	2.20±0.19	1.98±0.10	2.12±0.18	1.85±0.10	1.49±0.20
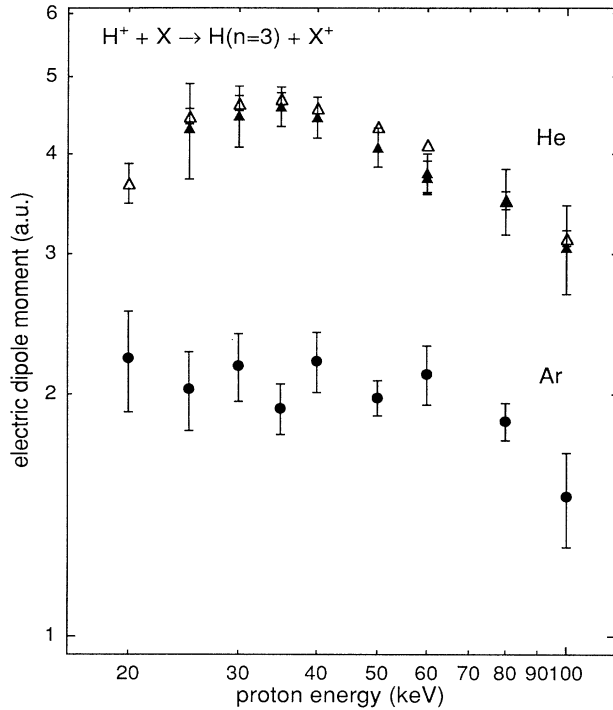
FIG. 8. The dipole moment for H($n = 3$) atoms produced by electron capture from both He and Ar targets: ●, present results for Ar; ▲, present results for He; △, previous results [3] with a different polarimeter for He.

The overall absolute uncertainty is 20% [17].

The $3s$ and $3p$ cross sections are compared with results from Hughes *et al.* [16], who made the only other measurements in this energy range. The comparison is shown in Fig. 9. Good agreement is seen for the $3s$ capture cross section. Agreement between the two sets of data for the $3p$ cross section is fair at high energies and poor at low energies.

3. Probability density

The probability density for the wave function describing the H atom can be calculated from the density-matrix
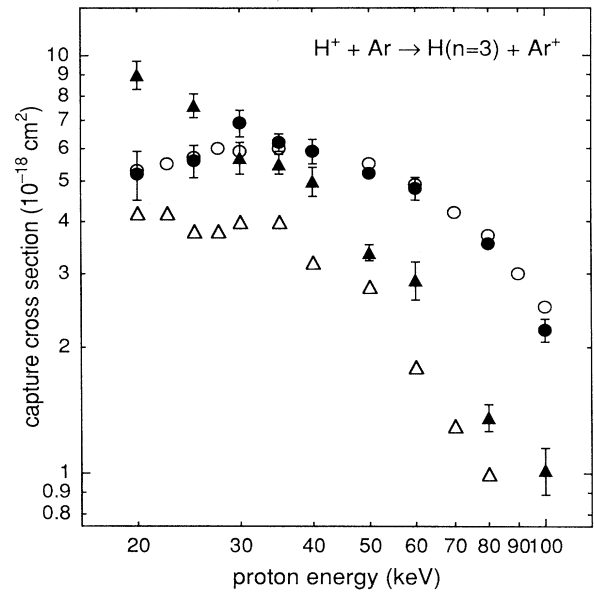
FIG. 9. Capture cross sections for protons on Ar: ●, capture to the $3s$ state, present results; ▲, capture to the $3p$ state, present results; ○, capture to the $3s$ state, Hughes *et al* [16]; △, capture to the $3p$ state, Hughes *et al.* The present results are obtained by normalizing the He relative cross sections to the work of Brower and Pipkin [17] and by correcting for different targets with a calibrated ion gauge. The error bars reflect random uncertainties only. The normalization adds an overall error of 20% [17]. The Hughes *et al.* results are absolute. For clarity, error bars for the Hughes results are not shown.

elements presented, as imaginary coherence terms do not contribute. Probability density graphs are shown in Figs. 10 and 11 for all collision energies. These display interesting qualitative differences with similar graphs obtained for the He target [3]. At high energies, the structure of the H atom probability density in the current work is similar to that from the He target. The electron cloud clearly lags behind the proton in both cases, with the difference that the cloud in the present results is stretched less. At 35 keV and below, however, a different structure is manifest in the atoms produced from the Ar

TABLE V. Cross sections for capture to the $3s$ and $3p$ states of H by protons on Ar. The relative cross sections are put on an absolute scale as describe din the text. The errors shown reflect only random uncertainty. The normalization from Brower and Pipkin [17] adds an overall 20% uncertainty. The cross sections are in 10^{-18} cm^2.

H$^+$ energy (keV)	$3s$ capture	$3p$ capture	$3d$ capture
20	5.2±0.7	9.0±0.7	3.3±1.1
25	5.6±0.5	7.6±0.5	2.1±0.9
30	6.9±0.5	5.7±0.5	1.7±0.8
35	6.2±0.3	5.5±0.3	1.7±0.8
40	5.9±0.4	5.0±0.4	0.9±0.7
50	5.22±0.18	3.37±0.15	0.6±0.3
60	4.8±0.3	2.9±0.3	0.3±0.5
80	3.54±0.11	1.36±0.10	0.21±0.18
100	2.20±0.14	1.02±0.13	0.07±0.24

target: the electron cloud not only lags behind the proton but also wraps around it to the sides, giving the cloud a horseshoe shape when viewed from above.

This is due to the relative prominence of p and d terms in the density matrix. Density matrices for H atoms produced from the He target were dominated at low energies by p diagonal terms and. $\mathrm{Re}(\sigma_{s0p0})$ coherence terms, which together gave the atom an elongated shape. The Ar target yields comparatively large $\sigma_{d\pm1}$ and $\mathrm{Re}(\sigma_{p\pm1d\pm1})$ terms, which give the atom a high electron density in the lobes on the sides. The consistent trend visible as beam energy is reduced lends credence to these results in spite of the poor determination of the σ_{d0} and $\sigma_{d\pm2}$ matrix elements.

4. Discussion

While theoretical calculations of the value of the H-atom dipole moment produced by electron capture from

He have been in reasonable agreement with experiment [35–37], there is little qualitative information available concerning the mechanism of dipole formation. While it is clear that the dipole is produced by the Coulomb field of the receding target ion following the collision, the detailed dynamics of the process are unclear.

Notice that while capture cross sections differ among the rare gases, generally rising as atomic number is increased, their behavior does not allow us to predict behavior of coherence terms. Parameters such as the dipole moment provide information about the collision that is not available in cross-section data. If one thinks of the dipole as a dynamical parameter controlled by the charge distribution of the projectile-target system, the comparison of results from He and Ar targets suggest some rough qualitative observations about the internuclear distance during the capture event. A limiting case of H-atom dipole formation would be at large internuclear distances—large enough that the newly formed H($n=3$)
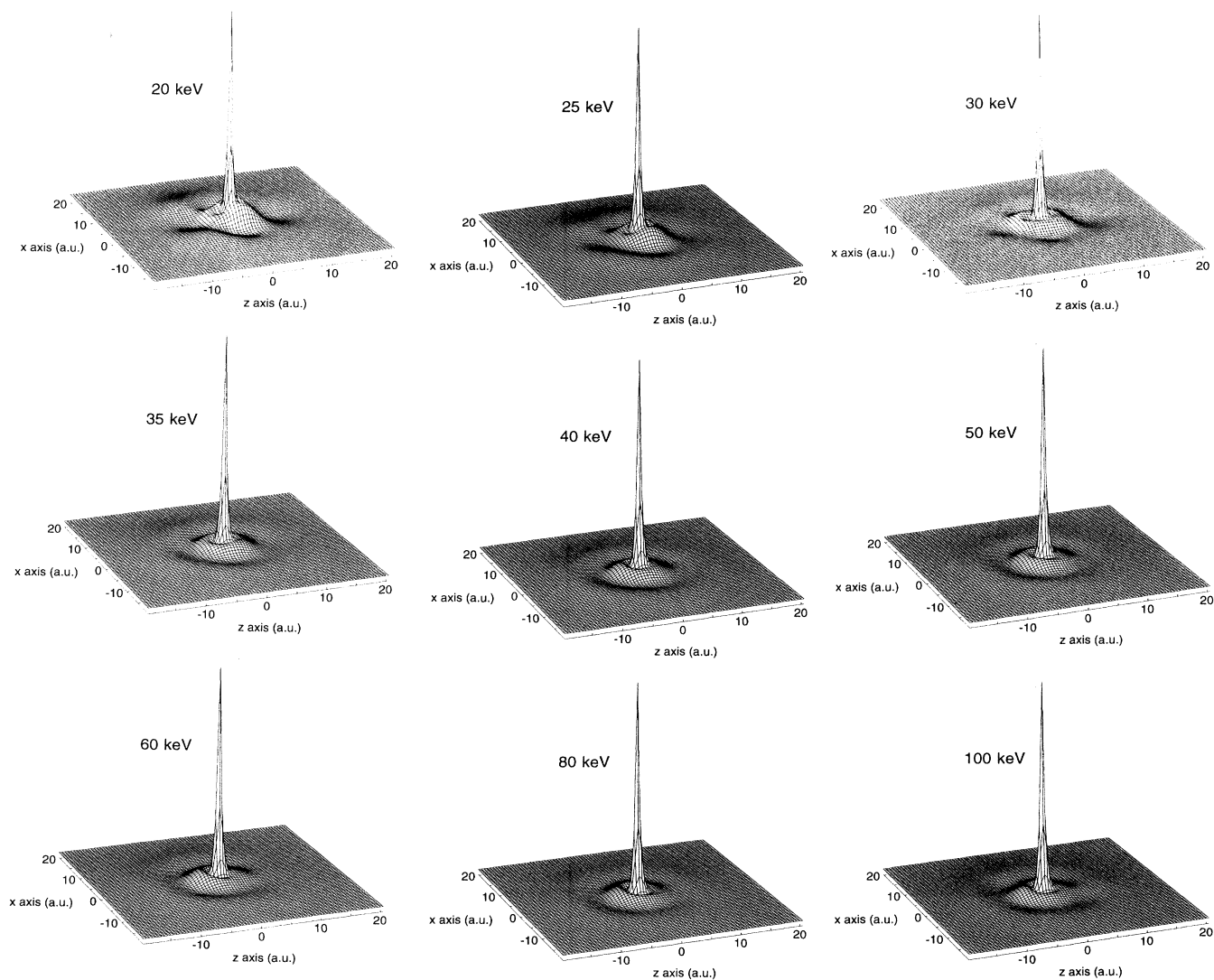

FIG. 10. Probability density in the x-z plane for the H atom. Density is indicated by height, with the vertical axis on each plot normalized to that plot's highest density. The beam direction is along the z axis, with the atom moving to the right.
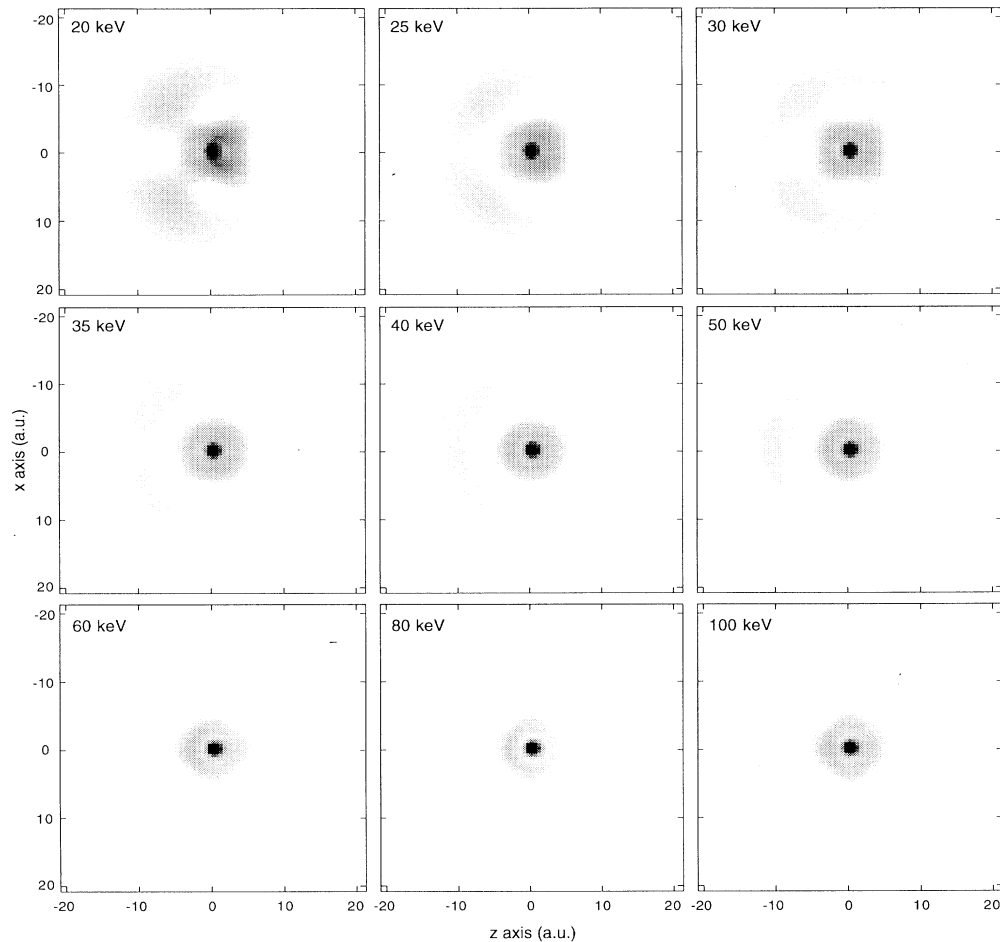
FIG. 11. Probability density in the x-z plane for the H atom. Here density is indicated by gray shading, with black areas indicating 20% of the maximum density on each plot and white areas indicating 0%. The truncated range is used to portray more clearly areas of low density. The z axis is horizontal, with the atom moving to the right. The displacement of the electron to the trailing side of the atom is clearly shown.

atom would simply be stretched by a receding ion of charge +1, with negligible differences between a receding He^+ and a receding Ar^+. This should result in the same dipole moment for H atoms produced from both targets. This is not the case. Rather, the different results for the two targets suggest that the proton penetrates the target sufficiently to produce significant charge distribution differences in the two collisions. The similarity between He and Ar target results at energies above 35 keV suggests strong similarities in the two collisions in that range, while the shifts in H($n = 3$)-atom charge distribu-

tion below 35 keV suggest that more complicated effects arise as projectile energy is reduced.

ACKNOWLEDGMENTS

*Present address: Department of Physics, North Central College, Naperville, IL 60566.
†Present address: Department of Computer Science, Mathematics, and Physics, Arkansas State University, State University, AR 72467.

[1] C. C. Havener, N. Rouze, W. B. Westerveld, and J. S. Risley, Phys. Rev. A 33, 276 (1986).
[2] J. R. Ashburn, R. A. Cline, C. D. Stone, P. J. M. van der Burgt, W. B. Westerveld, and J. S. Risley, Phys. Rev. A 40, 4885 (1989).
[3] J. R. Ashburn, R. A. Cline, P. J. M. van der Burgt, W. B. Westerveld, and J. S. Risley, Phys. Rev. A 41, 2407 (1990).
[4] R. A. Cline, W. B. Westerveld, and J. S. Risley (unpublished).
[5] F. Brouillard, Phys. Scr. 23, 163 (1981).
[6] R. Hippler, in Fundamental Processes in Atomic Collision

Physics, edited by H. Kleinpoppen, J. S. Briggs, and H. O. Lutz (Plenum, New York, 1985).

[7] R. Hippler, J. Phys. B **26**, 1 (1993).

[8] K. Blum, *Density Matrix Theory and Applications* (Plenum Press, New York, 1981).

[9] R. Hippler, W. Harbich, H. Madeheim, H. Kleinpoppen, and H. O. Lutz, Phys. Rev. A **35**, 3139 (1987).

[10] B. Van Zyl, M. W. Gealy, and H. Neumann, Phys. Rev. A **35**, 4551 (1987).

[11] R. Hippler, O. Plotzke, W. Harbich, H. Madeheim, H. Kleinpoppen, and H. O. Lutz, Phys. Rev. A **43**, 2587 (1991).

[12] G. Tepehan, B. Siegmann, H. Madeheim, and R. Hippler (unpublished).

[13] B. Van Zyl, H. L. Rothwell, Jr., and H. Neumann, Phys. Rev. A **21**, 730 (1980).

[14] B. Van Zyl, M. W. Gealy, and H. Neumann, Phys. Rev. A **33**, 2333 (1986).

[15] J. S. Risley, F. J. de Heer, and C. B. Kerkdijk, J. Phys. B **11**, 1759 (1978).

[16] R. H. Hughes, C. A. Stigers, B. M. Doughty, and E. D. Stokes, Phys. Rev. A **1**, 1424 (1970).

[17] M. C. Brower and F. M. Pipkin, Phys. Rev. A **39**, 3323 (1989).

[18] C. C. Havener, N. Rouze, W. B. Westerveld, and J. S. Risley, Phys. Rev. Lett. **53**, 1049 (1984).

[19] R. A. Cline, W. B. Westerveld, and J. S. Risley, Phys. Rev. A **43**, 1611 (1991).

[20] R. A. Cline, W. B. Westerveld, and J. S. Risley, Rev. Sci. Instrum. **64**, 1169 (1993).

[21] M. Billardon and J. Badoz, C. R. Acad. Sci., Ser. B **262**, 1672 (1966).

[22] J. C. Kemp, J. Opt. Soc. Am. **59**, 950 (1969).

[23] D. Clarke and J. F. Grainger, *Polarized Light and Optical Measurement* (Pergamon, Oxford, 1971).

[24] R. A. Stokes, P. A. Ekstrom, and J. B. Swedlund, Opt. Eng. **15**, 7 (1976).

[25] O. Acher, E. Bigan, and B. Drévillon, Rev. Sci. Instrum. **60**, 65 (1989).

[26] J. Badoz, M. P. Silverman, and J. C. Canit, J. Opt. Soc. Am. A **7**, 672 (1990).

[27] F. A. Modine and G. E. Jellison, Jr., Appl. Phys. Commun. **12**, 121 (1992).

[28] R. A. Cline, Ph.D. thesis, North Carolina State University, 1991.

[29] C. C. Havener, Ph.D. thesis, North Carolina State University, 1983.

[30] R. A. Mapleton, Phys. Rev. A **9**, 1013 (1974).

[31] S. Bashkin and J. O. Stoner, Jr., *Atomic Energy Levels and Grotrian Diagrams Vol. II: Sulfur I-Titanium XXII* (North-Holland, Amsterdam, 1978).

[32] W. L. Wiese, M. W. Smith, and B. M. Miles, Natl. Bur. Stand. (U.S.) Technical Report No. NSRDS-NBS-22 1969 (unpublished).

[33] S. L. Meyer, *Data Analysis for Scientists and Engineers* (Wiley, New York, 1975).

[34] P. R. Bevington, *Data Reduction and Error Analysis for the Physical Sciences* (Mc-Graw-Hill, New York, 1969).

[35] M. Kimura, Phys. Rev. A **44**, R5339 (1991).

[36] H. A. Slim, E. L. Heck, B. H. Bransden, and D. R. Flower, J. Phys. B **24**, 1683 (1991).

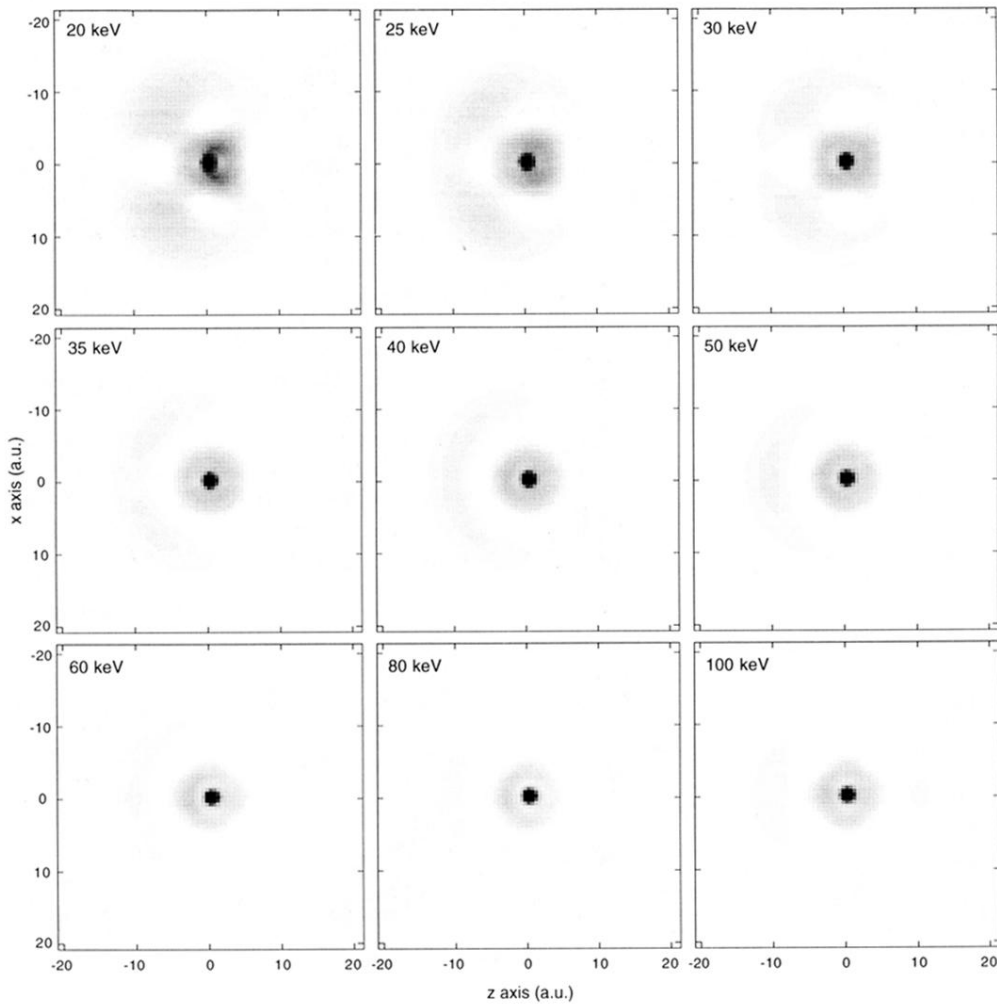[37] R. Shingal and C. D. Lin, J. Phys. B **24**, 963 (1991).

FIG. 11. Probability density in the x-z plane for the H atom. Here density is indicated by gray shading, with black areas indicating 20% of the maximum density on each plot and white areas indicating 0%. The truncated range is used to portray more clearly areas of low density. The z axis is horizontal, with the atom moving to the right. The displacement of the electron to the trailing side of the atom is clearly shown.